Electron-phonon coupling, critical temperatures, and gaps in $NbSe_2/MoS_2$ Ising superconductors

Shubham Patel,[1,*] Soumyasree Jena,[2] and A. Taraphder[1,†]
[1]*Department of Physics, Indian Institute of Technology, Kharagpur-721302, India*
[2]*Department of Chemistry, Indian Institute of Technology, Madras-600036, India*

(Received 5 January 2024; revised 21 June 2024; accepted 26 June 2024; published 10 July 2024)

Utilizing Migdal-Eliashberg theory of superconductivity within the first-principles calculations, we work out the role of electron-phonon coupling (EPC) and anisotropic superconducting properties of a recently discovered [Baidya *et al.*, Phys. Rev. B **104**, 174510 (2021)] 2D van der Waals heterostructure comprising a single layer of MoS_2 and few layers of $NbSe_2$. We find strong EPC and a softening of phonon modes in the lowest acoustic branch. While the single MoS_2 layer does not actively contribute to the EPC, it significantly elevates the superconducting critical temperature (T_c) compared to monolayer $NbSe_2$. This is attributed to the degradation of the charge-density wave by the MoS_2 layer. Notably, we observe a two-gap superconductivity in $NbSe_2/MoS_2$ and extend our study to three layers of $NbSe_2$. A reduction in T_c with increasing thickness of $NbSe_2$ is observed. Incorporation of spin-orbit coupling (SOC) suggests a possible mechanism for Ising superconductivity. We find that SOC reduces EPC while T_c is suppressed concomitantly by about 5K, leading to a closer estimate of the experimental T_c.

DOI: 10.1103/PhysRevB.110.014507

I. INTRODUCTION

Charge density wave (CDW) and superconductivity (SC) are competing instabilities in a vast variety of materials such as transition metal dichalcogenides (TMDs) [1,2], intercalated materials, and recently investigated Kagome metals [3]. TMDs have drawn great interest lately due to their device application potential. Apart from their semiconducting, spintronic, and valleytronic attributes, TMDs are studied for the competition between CDW and SC [4–11]. Other than disorder, dimensionality also plays a significant role in manipulating the behavior of these systems. [12,13].

Van der Waals heterostructures have captured considerable attention over the past two decades since the discovery of graphene due to the display of unique properties that hold immense promise for electronic and optoelectronic applications. The prospect of crafting a van der Waals heterostructure with intriguing emergent properties appears to be a unique route towards advanced tunable devices. In particular, the TMDs, which are categorized as two-dimensional semiconductors, have emerged as noteworthy candidates. Among these, MoS_2 has garnered substantial interest as a potential semiconductor, showcasing Ising superconductivity (ISC) in few-layer samples when subjected to electrostatic gating [14]. Likewise, $NbSe_2$ [15] represents another potential Ising superconductor. $NbSe_2$ and TaS_2/Se_2 had a long-standing appeal to experimental and theoretical investigators owing to the possible coexistence of CDW and SC [2,16]. Along with CDW and SC, ferromagnetism has also been reported in $NbSe_2$ [17], which makes it even more intriguing.

$2H-NbSe_2$ is a well-studied TMD material in which CDW and SC coexist at lower temperatures (CDW at 33K with coexisting SC below 7K) [18]. Electron-phonon coupling (EPC), along with electronic correlation [8], plays a crucial role in determining its instabilities. For $NbSe_2$, the phonon-softening along the ΓM direction of the Brillouin zone is usually considered a signature of CDW instability [1,12,15,19,20] in a large number of theoretical and experimental studies [7,21–24]. However, establishing a direct correlation between CDW and superconductivity is a matter of continued debate, often complicated by their occurrence at different regions of the Brillouin zone and the presence of disorder. The interpocket and intrapocket scatterings across the FS are proposed mechanisms for CDW and SC, respectively, in the monolayer system [25]. $2H-MoS_2$ is a very well-known member in the TMD family that has been studied quite extensively due to its large spin-orbit coupling (SOC) [26] and several other topological, electronic, optical, and catalytic properties.

It is found experimentally that 2D samples of $NbSe_2$ are unstable at ambient conditions. Also, theoretically, the high symmetry phase of $NbSe_2$ is predicted to be unstable. There is a transition to a distorted CDW 3×3 superstructure [12] as the temperature is reduced. In a recent study, ISC is claimed in the heterostacking of a few layers of $NbSe_2$ with a single layer of MoS_2, where the authors argue in favor of the stability of a 2D SC [27] state. Though the competition between CDW and SC was not addressed, it seems MoS_2 plays a very crucial role in mitigating the effects of CDW, stabilizing the SC state by preventing a clustering of $NbSe_2$ into a CDW superstructure, reported in an earlier study on intercalated $NbSe_2$ bilayers [28].

ISC has gained prominence as a burgeoning field in the search for unconventional SC lately [14,15,29,30]. ISC primarily originates in systems lacking inversion symmetry

*Contact author: spatelphy@iitkgp.ac.in
†Contact author: arghya@phy.iitkgp.ac.in

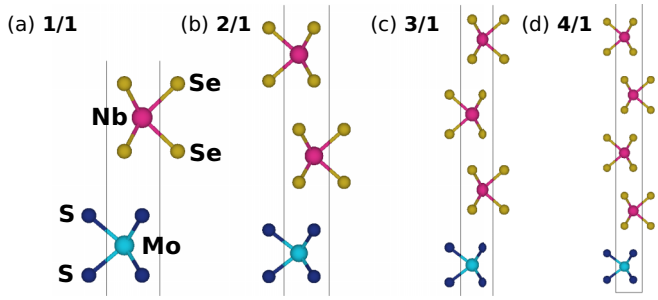

FIG. 1. The crystal structures of $NbSe_2/MoS_2$ (a) 1/1, (b) 2/1, (c) 3/1, and (d) 4/1 heterostructures. In all four cases, a single layer of MoS_2 and various layers of $NbSe_2$ are used. Magenta, yellow, cyan, and blue spheres, in the left figure, represent Nb, Se, Mo, and S atoms, respectively. A vacuum of 20 Å is introduced in all the geometries along the c axis.

that leads to an intrinsic SOC. TMDs are the main candidates in which ISC is likely to occur. In these systems, spins align themselves in the out-of-plane direction, and it takes a high in-plane upper critical field to destroy the superconductivity. For these superconductors, the in-plane magnetic field crosses the Chandrasekhar-Clogston-Pauli limit, $B_p = 1.86\,T_c$. Therefore, a considerable influence of SOC on the superconducting properties of Ising superconductors is anticipated. But SOC is not the only factor which affects ISC; spin-orbit scattering [31], singlet-triplet mixing [32], spin-fluctuations [33], disorder [34], and intervalley scattering [35] could affect ISC concurrently. In this paper, we will also discuss the effect of SOC on electronic and superconducting properties.

II. CRYSTAL STRUCTURES AND ELECTRONIC PROPERTIES

2H polymorphs of MoS_2 and $NbSe_2$ are members of the TMD family with D_{6h} point group symmetry in which transition metals are sandwiched between the chalcogen layers. We model 2D heterostructures with one layer of MoS_2 and n layers of $NbSe_2$ ($n/1$ configuration). MoS_2 with lattice constant (a) of 3.19 Å works as a substrate which produces ∼4% (for 1/1) of tensile strain while stacked with $NbSe_2$ ($a = 3.39$ Å). As the number of $NbSe_2$ layers is increased, the tensile strain in MoS_2 increases and reaches 6.48% in 4/1. The in-plane lattice constants and strain analysis for different layers of $(NbSe_2)_n/MoS_2$ are provided in Table T1 of the Supplemental Material (SM) [36]. The negative binding energy $[E_b(eV) = E_{NbSe_2/MoS_2} - E_{NbSe_2} - E_{MoS_2}]$ implies a strong possibility of the formation of $NbSe_2/MoS_2$ heterostructures as shown in Table T1 of the SM [36]. In the present paper, we go up to four layers of $NbSe_2$ that are stacked with MoS_2 in a particular stacking with respect to each other as shown in Fig. 1. It is important to mention that the AB stacking is used to form the crystal structures, which is found to be the most stable stacking for these hexagonal heterostructures [37]. In AB stacking, the chalcogen atom and the transition metal atom from different layers are on top of each other along the c axis. The monolayers of MoS_2 and $NbSe_2$ show semiconducting and metallic properties individually. $NbSe_2$ undergoes a structural transition to CDW phase at finite temperature (33K) and also shows superconducting properties at even lower temperature around 7K [25].

Electronic structure calculations show (see Fig. S1 in the SM [36]) that d orbitals of Nb atoms mainly contribute at the Fermi level (FL). The topology of the Nb bands is nearly intact close to the FL and remains the same as for the $NbSe_2$ monolayer, which is evident from the normalized density of states (DOS) [38,39] shown in Fig. S4 of SM [36]. Also, the overall band structure from MoS_2 layer is similar to the pristine monolayer, except the conduction bands are shifted downward and interact with the Nb bands, which clearly indicates interfacial interactions between the two layers at the interface. In the valence band region, one may notice a hybridization between Mo d orbitals and Se p orbitals. In the FS plot, there are two types of hole pockets, one at the Γ and the other at the K point. The emergence of the hole pocket at the Γ point is attributed to the Nb d_{z^2} orbital, whereas the hole pocket at the K point arises from the Nb $d_{x^2-y^2}$ and d_{xy} orbitals. Detailed atom and orbital projected band structures are provided in Figs. S1 and S2, respectively, of the SM [36]. Increasing the number of layers of $NbSe_2$ has no significant effect on the MoS_2 bands except shifting the MoS_2-derived bands downward as they cross the FL eventually for $n > 4$. The reason for this downward shift is the tensile strain induced in the heterostructures with increasing layers [37]. On the other hand, it is obvious that on increasing n, more bands populate the FL. The lowest band, which is closer to FL and belongs to the lowest $NbSe_2$ layer, comes closer to FL and becomes flatter, increasing the size of the hole pockets at the Γ point. Moreover, to understand the role of MoS_2 on the electronic properties near the interface, we calculate the band structures of the monolayer MoS_2 and multilayers of $NbSe_2$ separately. The red and blue plots in Fig. S3 represent monolayer MoS_2 and multilayers of $NbSe_2$, respectively. If we compare the band structures shown in Fig. S1(a) of the SM [36], we can see that the bands of MoS_2 are crossing the $(NbSe_2)_n$ bands close to the FL, which indicates that the MoS_2 bands affect the $NbSe_2$ bands, whereas the bands of a single layer MoS_2 and NbSe2 are quite separated (monolayer MoS_2 being a semiconductor) from each other if they are treated separately.

Next, we explore the impact of substituting one end layer of a multilayer $NbSe_2$ with MoS_2 on the electron transfer through Bader charge analysis [40]. In Fig. 2, we show the charge variation on each atomic species with (w) and without (w/o) the MoS2 layer, denoted as $\Delta e^- = e(A_{w/o-MoS_2}) - e(A_{w-MoS_2})$, where, A = Nb, Mo, Se, and S. A zero level indicates no disparity in total charge at a specific atom. Noticeably, significant differences emerge primarily around the MoS_2 layer due to distinct atomic numbers. Nonzero Δe^- values across all atomic species signify that the MoS_2 layer initiates charge transfer in the $(NbSe_2)_n/MoS_2$ system. Positive Δe^- implies charge depletion on that particular atom (transition metal) due to the presence of MoS_2, while the converse suggests charge accumulation (chalcogen). Ideally, replacing $NbSe_2$ with MoS_2 should cause charge variation solely in the bottom layer where $NbSe_2$ is replaced by the MoS_2 layer. However, Fig. 2 reveals a charge imbalance in other layers as well. This suggests that by replacing $NbSe_2$ with MoS_2, a large number of electrons are depleted and

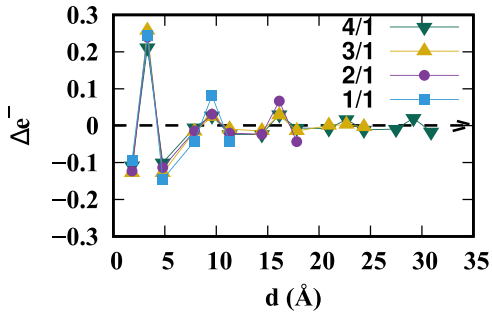

FIG. 2. The charge difference on each atomic species along the c axis, without and with MoS_2 layer for the four configurations shown on top right of the figure. Here, d represents the distance from the bottom of the supercell.

transferred from the bottom layer to the internal $NbSe_2$ region. In other words, holes from the internal Nb layers are transferred to MoS_2, leading to hole accumulation near the interface, yielding a two-dimensional hole gas (2DHG). From the electronic band structures (Fig. S1 of the SM [36]), it is evident that the bands crossing the Fermi level are mostly contributed by Nb d orbitals, forming a 2DHG. The chalcogen atoms have a meager contribution at the FL and therefore they affect the charge transfer mechanism minimally. Moreover, the charge imbalance inside $NbSe_2$ reduces gradually as one moves away from the MoS_2 layer. Beyond 8 Å, differences for Se atoms become negligible.

We also perform calculations including SOC. The SOC bands are shown in Fig. S1(c), where one may notice that SOC has a significant effect on $NbSe_2$ bands in all cases. Despite the significant spin-splitting observed in the bands of MoS_2, its considerable distance from the FL implies the splitting is not going to alter the physical picture substantially. The pair with red-black bands near the FL is closest to the interface and then there are the rest of the pairs away from the interface. It is interesting to note that this specific pair of bands exhibit Rashba SOC around the Γ point in all the cases. At the K point, the $NbSe_2$ bands at FL have a noticeable Zeeman-type spin splitting. This is similar to the case of monolayer MoS_2. This Rashba-type spin splitting in the bands near the interface is the signature of 2DEG at the interface of $NbSe_2$ and MoS_2. The rest of the pairs have negligible Rashba SOC as these band pairs are almost degenerate. The presence of SOC in van der Waals materials is pivotal in influencing electron-phonon interactions, which will be discussed later.

III. ANISOTROPIC SUPERCONDUCTING PROPERTIES

To calculate the phonon-mediated superconducting properties of the layered $NbSe_2/MoS_2$ heterostructure, we first calculate the dynamical matrices using density functional perturbation theory as implemented in QUANTUM ESPRESSO [41–43]. There is no visible gap in the spectrum over the whole frequency range. However, from the partial density of states it is clear that the lowest few phonon modes (acoustic) are contributed by Nb [the red curve in the phonon DOS for 1/1 of Fig. 3(d)], followed by a gap in the range between 15 to 20 meV for the Nb modes. All the modes coming from Nb in systems with $n > 1$ are equally populated in the acoustic

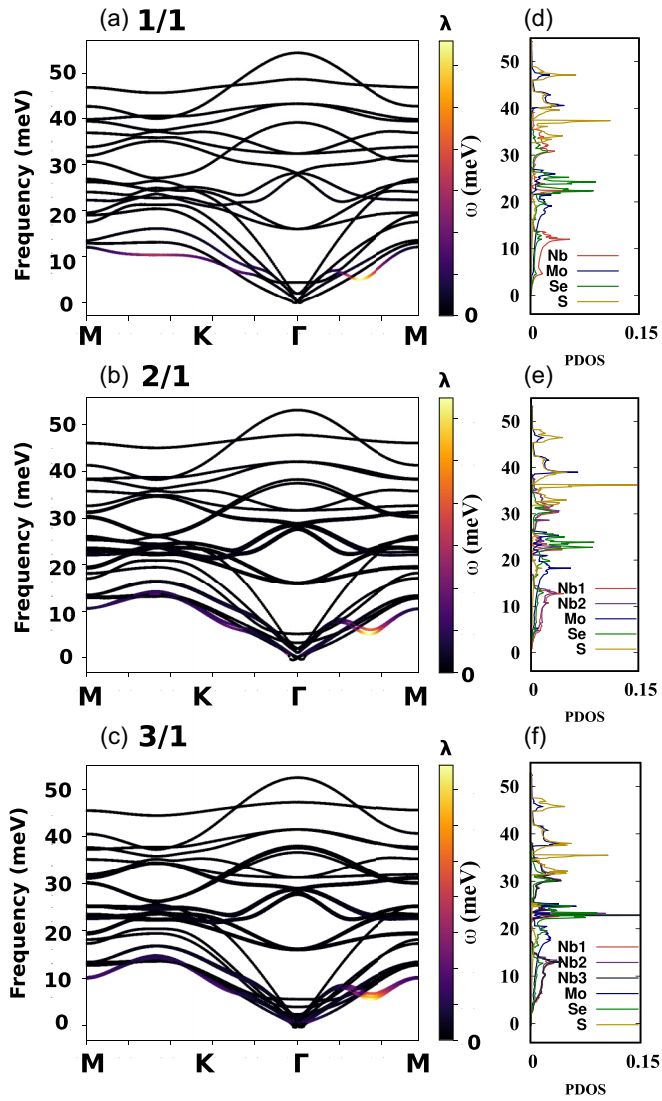

FIG. 3. (a)–(c) The phonon spectra and mode-resolved EPC for all three configurations. Absence of imaginary frequency in the phonon spectra implies stability of the heterostructures. The negligible softening around the Γ point is due to numerical artifact (see text). The softening along $\Gamma - M$ indicates a suppressed CDW. The color scale indicates the strength of EPC. (d)–(f) The partial DOS in the right panels.

phonon region in the range from 0 to 15 meV, as shown in Figs. 3(a)–3(c). There is a finite but very small contribution of the Mo atom to the acoustic modes in comparison to contributions from $NbSe_2$. The optical branches are coming mainly from S, and the Mo atom has a substantial contribution in the higher frequency regime. There is a small hybridization of Se with Nb in the acoustic modes, which suggests that the $NbSe_2$ layers play a substantial role in EPC. One can also note that beyond 35 meV, neither Nb nor Se contributes to the optical branches, and it will be more explicit in the spectral function plot shown in Fig. 4, that, beyond 35 meV, $\alpha^2F(\omega)$ vanishes. This implies $NbSe_2$ layers only are responsible for EPC and electron-phonon induced SC. The plots of mode-resolved $\alpha^2F(\omega)$ (Fig. S8 in the SM [36]) vindicates this clearly. These plots and details thereof are provided in Fig. S1 of the SM

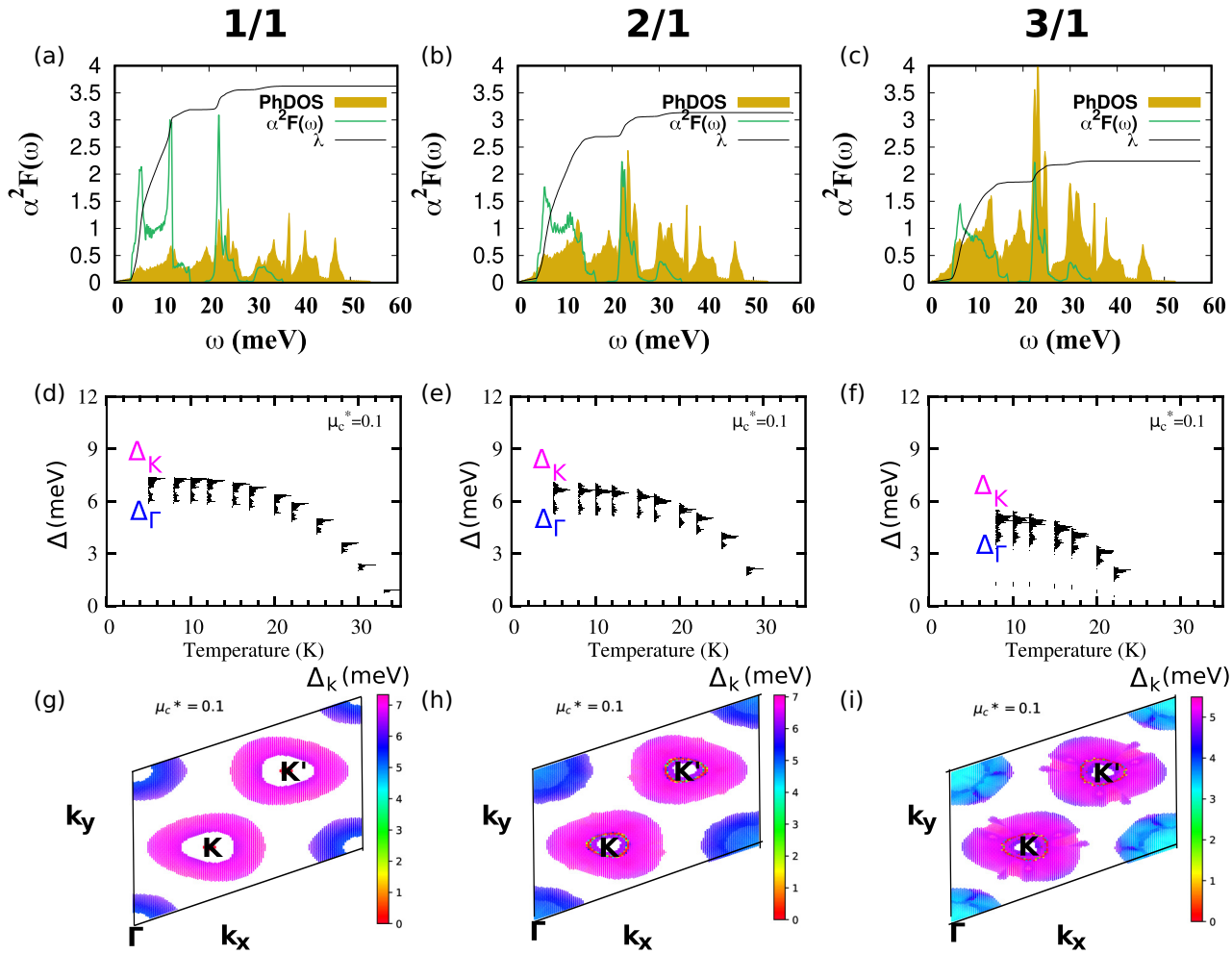

FIG. 4. The Eliashberg spectral function [$\alpha^2F(\omega)$, green] along with the integrated EPC strength (λ, black) for (a) 1/1, (b) 2/1, and (c) 3/1 structures. The phonon DOS is in yellow. (d)–(f) The energy distribution of the gap (Δ) as a function of temperature at $\mu_c^* = 0.1$. Δ_K and the Δ_Γ are the gap distributions around the K and Γ points, respectively. The two-gap nature is clear from the gap-resolved FS (g)–(i) plotted at $T = 8$ K; the nature remains the same for other temperatures.

[36]. To be sure of the source of EPC, mode-resolved electron-phonon linewidth plots are also shown in Fig. 3, using the relation [44,45],

$$\lambda_{qv} = \frac{1}{N(\epsilon_F)\omega_{qv}} \sum_{nm} \int_{\mathrm{BZ}} \frac{dk}{\Omega_{\mathrm{BZ}}} |g_{mn,v}(k,q)|^2 \times \delta(\epsilon_{nk} - \epsilon_F)\delta(\epsilon_{mk+q} - \epsilon_F). \quad (1)$$

The parameters are defined in the computational details section of the SM [36] (see also Refs. [46–49] therein). One can clearly observe a phonon-softening in between Γ and M high-symmetry points in the LA phonon branch, which is known to be the E' vibrational mode of the acoustic branch. This mode belongs to the $NbSe_2$ layer and indicates the movement of Nb and two Se atoms in the same in-plane direction. It is interesting to point out that in bulk $NbSe_2$, this phonon softening occurs at a $\mathbf{q}$ point, where $\mathbf{q} = \frac{2}{3}\Gamma M$ [12,25,50], implying a 3×3 CDW instability. In the case of 1/1-$NbSe_2/MoS_2$, we observe it at $\mathbf{q} = \frac{1}{2}\Gamma M$ [(Fig. 3(a)], suggesting a commensurate 4×4 CDW ordering. This is similar to the case of monolayer $NbSe_2$, where the phonon-softening occurs at $= \frac{1}{2}\Gamma M$ [12,33]. As the number of $NbSe_2$ layers increases, the softening approaches bulk value, $\mathbf{q} = \frac{2}{3}\Gamma M$, gradually, possibly through a series of incommensurate CDWs, at least for 2/1 and 3/1 configurations. The color scale suggests that almost all the EPC is concentrated in this phonon-softening valley of the acoustic branch of $NbSe_2$ and the other modes do not contribute to EPC. This is true for all the three cases of Figs. 3(a)–3(c).

Next we calculate EPC strength, λ, as a function of frequency, shown in Fig. 4(a), along with Eliashberg spectral function $\alpha^2F(\omega)$. $\alpha^2F(\omega)$ vanishes beyond 35 meV. Comparison of $\alpha^2F(\omega)$ with partial DOS [in Figs. 3(d)–3(f)] shows that the contribution from $NbSe_2$ layers also vanishes beyond this range; which means $NbSe_2$ layers are the sole contributors to EPC. The $\alpha^2F(\omega)$ also behaves in the same manner as the partial DOS in the range 0−35 meV. The gaps in $\alpha^2F(\omega)$ in the range 15−20 meV and 25−30 meV in Figs. 4(a)–4(c) are apparent from the partial DOS of Nb and Se in Figs. 3(d)–3(f). The cumulative EPC, indicated by λ in

TABLE I. Variation of T_c with lowest, moderate, and highest possible values of Coulomb potential, μ_c^*. T_c reduces with increasing μ_c^*; λ is EPC strength.

μ_c^*	T_c (K)		
	1/1	2/1	3/1
	$\lambda = 3.52$	$\lambda = 3.13$	$\lambda = 2.24$
0.05	37.4	34.1	28.7
0.10	35.3	31.0	24.0
0.16	30.1	27.9	21.3

Figs. 4(a)–4(c), is calculated using Eq. (2), described in the SM [36]. Clearly, λ reduces from 3.52 to 2.4 as the $NbSe_2$ layer numbers increase from 1 to 3 (i.e., 1/1 to 3/1 heterostructure), respectively, due to the reduction of $\alpha^2F(\omega)$. This reduction in total EPC will also result in the reduction of T_c. A sudden jump in λ at a frequency, $\omega = 23$ meV, is noticed in all three cases, due to a gap opening in the spectral function between acoustic and optical phonon modes of Nb.

To evaluate the superconducting T_c, fully anisotropic Migdal-Eliashberg theory [44,51,52] is employed. Figures 4(d)–4(f) show the energy distribution of the superconducting gap as a function of temperature at an effective Coulomb potential $\mu^* = 0.1$. The leading edge of the gap function (Δ_0) at $T = 0$ K is at 6.7 meV. The ordinary Allen-Dynes modified McMillan equation [53–55] gives a superconducting $T_c = 20$ K, while anisotropic Migdal-Eliashberg theory gives $T_c = 35$ K. This large difference in the two superconducting T_c is a signature of anisotropy in the superconducting gap distribution on the FS, which is a consequence of the multisheet nature of FS in $NbSe_2/MoS_2$. This was observed [44] in MgB_2 ($T_c = 39$ K) too, which is a two-gap superconductor. In $NbSe_2/MoS_2$, there are hole pockets around Γ, K, and K' valleys in the BZ. The larger gap is associated with the in-plane $d_{x^2-y^2}$ and d_{xy} Fermi sheets at the $K(K')$ point, while the smaller gap involves out-of-plane Nb d_{z^2} Fermi sheets located around the Γ point, shown in the gap-resolved FS in Figs. 4(g)–4(i). It is interesting to note that the two-gap feature is robust with increasing number of $NbSe_2$ layers. The anisotropy in the superconducting gap function can also be realized by the typical BCS relation, $2\Delta_0 = 3.52k_BT_c$. Our analysis reveals deviation from this typical ratio, with values 4.47, 4.64, and 4.35 for 1/1, 2/1, and 3/1 heterostructures, respectively. This disparity indicates unconventional SC in $NbSe_2/MoS_2$. It is possible that other mechanisms are also at play here such as magnetic interactions [32] and spin fluctuations [33].

The calculated T_c of $NbSe_2/MoS_2$ is large compared to a single layer of $NbSe_2$. The experimental value is 3.8 K for the single layer system [56], while it is 7 K for bulk $NbSe_2$ [57]. The electron-phonon calculations based on Migdal-Eliashberg theory (details in the SM [36]) on a 3x3 CDW supercell reported $T_c = 4.4$ K for a single layer [25]. Thus, our study suggests that a single layer of MoS_2 has a substantial impact on SC of 2H-$NbSe_2$. Increasing the number of $NbSe_2$ layers up to three shows a constant reduction in T_c in Figs. 4(d)–4(f) and in Table I. T_c is sensitive to the choice of Coulomb potential (μ_c^*). An increase in μ_c^* results in a decrease in superconducting Δ_0 and T_c [44]. Since there are no available estimates of μ_c^* to compare with, we have calculated T_c for different values of μ_c^* (Table I).

TABLE II. Variation of T_c for $NbSe_2$ (i.e., without including MoS_2 monolayer) but keeping the lattice constants similar to that in the heterostructures with MoS_2. Here, a is the in-plane lattice constant and compressive and tensile indicate the reduced and enhanced lattice constant regimes for various configurations ($\mu_c^* = 0.1$).

Configuration	Compressive (c)		Tensile (t)	
Unstrained $NbSe_2$				
($T_c = 20$ K)	a(Å)	T_c (K)	a(Å)	T_c (K)
$(NbSe_2)_1$	3.31	34	3.65	17.5
$(NbSe_2)_2$	3.36	29	3.61	18.05
$(NbSe_2)_3$	3.38	26	3.59	20

ISC with $T_c \simeq 6.5$ K has been suggested in a single layer of MoS_2 stacked with a few layers of $NbSe_2$ (~15 nm, to be exact) [27,58] recently. A similar T_c is expected with increasing $NbSe_2$ layers. The variation of T_c with the thickness of $NbSe_2$ suggests an increase in $NbSe_2$ layers will result in a suppression of T_c as shown in scanning tunneling microscopy measurements [59]. This paper emphasizes the use of high-quality samples, possibly less influenced by environmental factors, such as oxidation or defects, which could have affected the earlier results, particularly those prepared on SiO_2/Si substrates [15,18]. On the other hand, our findings attribute the variation in T_c solely to electron-phonon interactions, demonstrating a reduction in electron-phonon coupling strength with increasing layer thickness, directly impacting T_c. Migdal-Eliashberg theory, incorporating spin fluctuations, finds this trend for 1H-TaS_2 [13,60] and more recently in 2H-$NbSe_2$ [33]. In 1H-TaS_2, it is attributed to an inevitable suppression of Cooper pair density at the superconductor-vacuum interface. Our computational resources make it difficult to go beyond three layers of $NbSe_2$, however, the trend is clear. To delineate the role of MoS_2, we perform electron-phonon and superconductivity calculations for all three configurations without the MoS_2 layer. We considered both compressive and tensile strains (albeit the experimental strain being compressive only), with the compressions matching the observed values in the 1/1, 2/1, and 3/1 heterostructures with MoS_2. The band structures for the strained $NbSe_2$ are shown in Fig. S7 of the SM [36]. There is no significant change in the band structures at the Fermi level, just the positions of the valence band maximum (VBM) are changed while moving from compressive to tensile strains. As shown in Fig. S7(a) and S7(d), the VBM for $(NbSe_2)_1$ is shifted from the K point to the Γ point. The same is true for $(NbSe_2)_2$ [Figs. S7(b) and S7(e)] and $(NbSe_2)_3$ [Figs. S7(c) and S7(f)]. Additionally, with close inspection, one can notice that the size of the Fermi surface sheets around the Γ point for all the strained geometries are larger compared to the $(NbSe_2)_n/MoS_2$ heterostructures.

Our findings indicate that a multilayer $NbSe_2$ under compression has similar superconducting T_c as the $NbSe_2/Mos_2$ heterostructure, suggesting that the major contribution of MoS_2 is to provide a compressive strain on $NbSe_2$ affecting the EPC (see Table II). Furthermore, without the MoS_2 layer, there is phonon softening around the Γ point (other than along

ΓM), as shown in Figs. S5(a)– S5(c) of the SM [36], which has minimal impact on the superconducting T_c. It is also evident that the critical temperature T_c consistently decreases from compressive to tensile strain regimes (see Table II and Fig. S6 [36]). The phonon softening around the Γ point disappears for tensile strain. Moreover, the CDW softening along $\Gamma - M$ diminishes with the reduced number of layers and increasing lattice constant for every configuration. Finally, despite the reduction in phonon softening with increased lattice constant, T_c decreases. This decrease might be attributed to the considerable reduction in EPC strength in the tensile regime (see the color scale in Fig. S5 [36]). Further experimental evidences are necessary to confirm the behavior of CDW instability in this regime. The Migdal-Eliashberg approach results in fair agreement for a variety of materials, though it overestimates the superconducting gap and T_c [32,33,50]. There exist claims that in $NbSe_2$ and similar materials that show ISC, the overestimation of phonon-induced SC can be mitigated by spin fluctuations [32,33]. For comparison, we perform the anisotropic superconducting calculations for the $NbSe_2$ monolayer and find an overestimated $T_c = 20$ K as reported earlier [33]. The same could be possible for $NbSe_2/MoS_2$ heterostructures.

Finally, speaking of ISC, a mechanism which is controlled by SOC in noncentrosymmetric materials, we notice that the SOC, which has been ignored in electron-phonon calculations so far, can have a huge impact on the EPC strength. Inclusion of SOC weakens the EPC strength almost by a factor of 2 as reported earlier in the case of $CaBi_2$ [61] and TaS_2 [60], close to the experimentally reported values. The $(NbSe_2)_n/MoS_2$ system exhibits a reasonable SOC as illustrated in Fig. S1(c), which is evident from the Zeeman-type spin splitting at the K point in the BZ. Considering this, incorporating SOC into calculations may yield a more accurate estimate of T_c. Including SOC, the superconducting T_c is indeed reduced by about 5 K for 1/1 ($T_c = 30$ K, $\lambda = 3.32$) and 2/1-$NbSe_2/MoS_2$ ($T_c = 26.6$ K, $\lambda = 2.57$) as shown in Fig. S9 of the SM [36]. More experimental investigations should provide a better estimate of T_c in $(NbSe_2)_n/MoS_2$ (<15 nm) and validate our results.

IV. CONCLUSIONS

To summarize, we investigated electronic and superconducting properties of AB-stacked $NbSe_2/MoS_2$ van der Waals heterostructures and studied the behavior of critical temperature T_c with the number of layers of $NbSe_2$, using Migdal-Eliashberg theory. While $NbSe_2$ layers affect the FL considerably, a single layer of MoS_2 does not significantly alter the FS topology, at least up to 4/1 configuration. Moreover, the heterostructure shows a robust EPC strength. A pronounced phonon softening in the acoustic modes of the $NbSe_2$ layers is observed along the $\Gamma - M$ direction, attributed to movements of Nb and Se atoms within the *ab* plane. MoS_2 layers do not exhibit any EPC, though their inclusion dramatically enhances the T_c when stacked with $NbSe_2$. This enhancement owes its origin to the stabilization of the crystal structure by MoS_2, mitigating the CDW instability of $NbSe_2$. Our findings suggest a substantial increase in T_c when a semiconducting 2D material like MoS_2 is combined with a superconducting counterpart like $NbSe_2$. In the heterostructures, the major role of MoS_2 appears to produce a compressive strain on $NbSe_2$, affecting EPC and T_c. We also suggest that increasing the thickness of $NbSe_2$, stacked with a single layer of MoS_2, results in an unusual reduction in T_c. We anticipate that the experimentally reported T_c could be attained by adding more (beyond four) layers of $NbSe_2$. Additionally, we observe that the inclusion of SOC leads to a marked decrease in EPC, significantly degrading T_c. This also points to the possibility of an Ising superconductivity in this system.

ACKNOWLEDGMENTS

We acknowledge the National Supercomputing Mission (NSM) for providing computing resources of PARAM Shakti at IIT Kharagpur, which is implemented by C-DAC and supported by the Ministry of Electronics and Information Technology (MeitY) and Department of Science and Technology (DST), Government of India.

[1] M. M. Ugeda, A. J. Bradley, Y. Zhang, S. Onishi, Y. Chen, W. Ruan, C. Ojeda-Aristizabal, H. Ryu, M. T. Edmonds, H.-Z. Tsai *et al.*, Characterization of collective ground states in single-layer $NbSe_2$, Nat. Phys. **12**, 92 (2016).

[2] S. Koley, N. Mohanta, and A. Taraphder, Charge density wave and superconductivity in transition metal dichalcogenides, Eur. Phys. J. B **93**, 77 (2020).

[3] F. Yu, D. Ma, W. Zhuo, S. Liu, X. Wen, B. Lei, J. Ying, and X. Chen, Unusual competition of superconductivity and charge-density-wave state in a compressed topological kagome metal, Nat. Commun. **12**, 3645 (2021).

[4] G. Grüner, The dynamics of charge-density waves, Rev. Mod. Phys. **60**, 1129 (1988).

[5] S. V. Borisenko, A. A. Kordyuk, V. B. Zabolotnyy, D. S. Inosov, D. Evtushinsky, B. Büchner, A. N. Yaresko, A. Varykhalov, R. Follath, W. Eberhardt, L. Patthey, and H. Berger, Two energy gaps and Fermi-surface "arcs" in $NbSe_2$, Phys. Rev. Lett. **102**, 166402 (2009).

[6] R. E. Thomson, B. Burk, A. Zettl, and J. Clarke, Scanning tunneling microscopy of the charge-density-wave structure in 1T-TaS_2, Phys. Rev. B **49**, 16899 (1994).

[7] F. Weber, S. Rosenkranz, J.-P. Castellan, R. Osborn, R. Hott, R. Heid, K.-P. Bohnen, T. Egami, A. H. Said, and D. Reznik, Extended phonon collapse and the origin of the charge-density wave in 2*H*-$NbSe_2$, Phys. Rev. Lett. **107**, 107403 (2011).

[8] S. Dordevic, D. Basov, R. Dynes, B. Ruzicka, V. Vescoli, L. Degiorgi, H. Berger, R. Gaál, L. Forró, and E. Bucher, Optical properties of the quasi-two-dimensional dichalcogenides 2*H*-TaSe and 2*H*-NbSe, Eur. Phys. J. B **33**, 15 (2003).

[9] A. Taraphder, S. Koley, N. S. Vidhyadhiraja, and M. S. Laad, Preformed excitonic liquid route to a charge density wave in 2*H*-$TaSe_2$, Phys. Rev. Lett. **106**, 236405 (2011).

[10] S. Koley, M. S. Laad, N. S. Vidhyadhiraja, and A. Taraphder, Preformed excitons, orbital selectivity, and charge density wave order in 1T-$TiSe_2$, Phys. Rev. B **90**, 115146 (2014).

[11] P. Dreher, W. Wan, A. Chikina, M. Bianchi, H. Guo, R. Harsh, S. Manas-Valero, E. Coronado, A. J. Martínez-Galera, P. Hofmann *et al.*, Proximity effects on the charge density wave order and superconductivity in single-layer $NbSe_2$, ACS Nano **15**, 19430 (2021).

[12] M. Calandra, I. I. Mazin, and F. Mauri, Effect of dimensionality on the charge-density wave in few-layer 2*H*-$NbSe_2$, Phys. Rev. B **80**, 241108(R) (2009).

[13] C.-S. Lian, Interplay of charge ordering and superconductivity in two-dimensional 2*H* group V transition-metal dichalcogenides, Phys. Rev. B **107**, 045431 (2023).

[14] J. Lu, O. Zheliuk, I. Leermakers, N. F. Yuan, U. Zeitler, K. T. Law, and J. Ye, Evidence for two-dimensional Ising superconductivity in gated MoS_2, Science **350**, 1353 (2015).

[15] X. Xi, Z. Wang, W. Zhao, J.-H. Park, K. T. Law, H. Berger, L. Forró, J. Shan, and K. F. Mak, Ising pairing in superconducting $NbSe_2$ atomic layers, Nat. Phys. **12**, 139 (2016).

[16] D. C. Freitas, P. Rodière, M. R. Osorio, E. Navarro-Moratalla, N. M. Nemes, V. G. Tissen, L. Cario, E. Coronado, M. García-Hernández, S. Vieira, M. Núñez-Regueiro, and H. Suderow, Strong enhancement of superconductivity at high pressures within the charge-density-wave states of 2*H*-TaS_2 and 2*H*-$TaSe_2$, Phys. Rev. B **93**, 184512 (2016).

[17] X. Zhu, Y. Guo, H. Cheng, J. Dai, X. An, J. Zhao, K. Tian, S. Wei, X. Cheng Zeng, C. Wu *et al.*, Signature of coexistence of superconductivity and ferromagnetism in two-dimensional $NbSe_2$ triggered by surface molecular adsorption, Nat. Commun. **7**, 11210 (2016).

[18] X. Xi, L. Zhao, Z. Wang, H. Berger, L. Forró, J. Shan, and K. F. Mak, Strongly enhanced charge-density-wave order in monolayer $NbSe_2$, Nat. Nanotechnol. **10**, 765 (2015).

[19] T. Valla, A. V. Fedorov, P. D. Johnson, P.-A. Glans, C. McGuinness, K. E. Smith, E. Y. Andrei, and H. Berger, Quasiparticle spectra, charge-density waves, superconductivity, and electron-phonon coupling in 2*H*-$NbSe_2$, Phys. Rev. Lett. **92**, 086401 (2004).

[20] F. Zheng, Z. Zhou, X. Liu, and J. Feng, First-principles study of charge and magnetic ordering in monolayer $NbSe_2$, Phys. Rev. B **97**, 081101(R) (2018).

[21] N. Doran, A calculation of the electronic response function in 2*H*-$NbSe_2$ including electron-phonon matrix element effects, J. Phys. C **11**, L959 (1978).

[22] M. D. Johannes, I. I. Mazin, and C. A. Howells, Fermi-surface nesting and the origin of the charge-density wave in $NbSe_2$, Phys. Rev. B **73**, 205102 (2006).

[23] M. D. Johannes and I. I. Mazin, Fermi surface nesting and the origin of charge density waves in metals, Phys. Rev. B **77**, 165135 (2008).

[24] C. J. Arguello, E. P. Rosenthal, E. F. Andrade, W. Jin, P. C. Yeh, N. Zaki, S. Jia, R. J. Cava, R. M. Fernandes, A. J. Millis, T. Valla, R. M. Osgood, and A. N. Pasupathy, Quasiparticle interference, quasiparticle interactions, and the origin of the charge density wave in 2*H*-$NbSe_2$, Phys. Rev. Lett. **114**, 037001 (2015).

[25] F. Zheng and J. Feng, Electron-phonon coupling and the coexistence of superconductivity and charge-density wave in monolayer $NbSe_2$, Phys. Rev. B **99**, 161119(R) (2019).

[26] Z. Y. Zhu, Y. C. Cheng, and U. Schwingenschlögl, Giant spin-orbit-induced spin splitting in two-dimensional transition-metal dichalcogenide semiconductors, Phys. Rev. B **84**, 153402 (2011).

[27] P. Baidya, D. Sahani, H. K. Kundu, S. Kaur, P. Tiwari, V. Bagwe, J. Jesudasan, A. Narayan, P. Raychaudhuri, and A. Bid, Transition from three- to two-dimensional Ising superconductivity in few-layer $NbSe_2$ by proximity effect from van der Waals heterostacking, Phys. Rev. B **104**, 174510 (2021).

[28] Y. Yin, C.-S. Lian, F. Meng, Y. Liu, W. Chen, L. Ji, X. Zhou, Z. Zhang, Q. Zhang, L. Gu, W. Duan, Q.-K. Xue, X. Chen, and S.-H. Ji, Quenched charge density wave and large in-plane upper critical field of self-intercalated bilayer $NbSe_2$, Phys. Rev. B **108**, L041405 (2023).

[29] S. C. De la Barrera, M. R. Sinko, D. P. Gopalan, N. Sivadas, K. L. Seyler, K. Watanabe, T. Taniguchi, A. W. Tsen, X. Xu, D. Xiao *et al.*, Tuning Ising superconductivity with layer and spin–orbit coupling in two-dimensional transition-metal dichalcogenides, Nat. Commun. **9**, 1427 (2018).

[30] B. T. Zhou, N. F. Q. Yuan, H.-L. Jiang, and K. T. Law, Ising superconductivity and Majorana fermions in transition-metal dichalcogenides, Phys. Rev. B **93**, 180501(R) (2016).

[31] R. V. Coleman, G. K. Eiserman, S. J. Hillenius, A. T. Mitchell, and J. L. Vicent, Dimensional crossover in the superconducting intercalated layer compound 2*H*-TaS_2, Phys. Rev. B **27**, 125 (1983).

[32] D. Wickramaratne, S. Khmelevskyi, D. F. Agterberg, and I. I. Mazin, Ising superconductivity and magnetism in $NbSe_2$, Phys. Rev. X **10**, 041003 (2020).

[33] S. Das, H. Paudyal, E. R. Margine, D. F. Agterberg, and I. I. Mazin, Electron-phonon coupling and spin fluctuations in the Ising superconductor $NbSe_2$, npj Comput. Mater. **9**, 66 (2023).

[34] D. Möckli and M. Khodas, Ising superconductors: Interplay of magnetic field, triplet channels, and disorder, Phys. Rev. B **101**, 014510 (2020).

[35] S. Ilić, J. S. Meyer, and M. Houzet, Enhancement of the upper critical field in disordered transition metal dichalcogenide monolayers, Phys. Rev. Lett. **119**, 117001 (2017).

[36] See Supplemental Material at http://link.aps.org/supplemental/10.1103/PhysRevB.110.014507 for computational details; The electronic structures, strain analysis, role of MoS_2 on electronic and superconducting properties; The mode-resolved spectral function plots are shown in detail; The plots of superconducting gap functions with SOC are also provided; and which contains Refs. [41–43,46–49,51,53,55,62,63].

[37] S. Patel, U. Dey, N. P. Adhikari, and A. Taraphder, Electric field and strain-induced band-gap engineering and manipulation of the Rashba spin splitting in Janus van der Waals heterostructures, Phys. Rev. B **106**, 035125 (2022).

[38] J. Shi, D. Le, V. Turkowski, N. U. Din, T. Jiang, Q. Gu, and T. S. Rahman, Thickness dependence of superconductivity in FeSe films, Eur. Phys. J. Plus **138**, 505 (2023).

[39] A. Linscheid, Electronic properties of the FeSe/STO interface from first-principle calculations, Supercond. Sci. Technol. **29**, 104005 (2016).

[40] G. Henkelman, A. Arnaldsson, and H. Jónsson, A fast and robust algorithm for Bader decomposition of charge density, Comput. Mater. Sci. **36**, 354 (2006).

[41] P. Giannozzi, S. Baroni, N. Bonini, M. Calandra, R. Car, C. Cavazzoni, D. Ceresoli, G. L. Chiarotti, M. Cococcioni, I. Dabo *et al.*, QUANTUM ESPRESSO: A modular and open-source software project for quantum simulations of materials, J. Phys.: Condens. Matter **21**, 395502 (2009).

[42] P. Giannozzi, O. Andreussi, T. Brumme, O. Bunau, M. B. Nardelli, M. Calandra, R. Car, C. Cavazzoni, D. Ceresoli, M. Cococcioni *et al.*, Advanced capabilities for materials modelling with quantum espresso, J. Phys.: Condens. Matter **29**, 465901 (2017).

[43] P. Giannozzi, O. Baseggio, P. Bonfà, D. Brunato, R. Car, I. Carnimeo, C. Cavazzoni, S. De Gironcoli, P. Delugas, F. Ferrari Ruffino *et al.*, QUANTUM ESPRESSO toward the exascale, J. Chem. Phys. **152**, 154105 (2020).

[44] E. R. Margine and F. Giustino, Anisotropic Migdal-Eliashberg theory using Wannier functions, Phys. Rev. B **87**, 024505 (2013).

[45] H. Lee, S. Poncé, K. Bushick, S. Hajinazar, J. Lafuente-Bartolome, J. Leveillee, C. Lian, F. Macheda, H. Paudyal, W. H. Sio *et al.*, Electron-phonon physics from first principles using the EPW code, Nature Comput. Mater. **9**, 156 (2023).

[46] J. P. Perdew, K. Burke, and M. Ernzerhof, Generalized gradient approximation made simple, Phys. Rev. Lett. **77**, 3865 (1996).

[47] P. E. Blöchl, Projector augmented-wave method, Phys. Rev. B **50**, 17953 (1994).

[48] G. Kresse and D. Joubert, From ultrasoft pseudopotentials to the projector augmented-wave method, Phys. Rev. B **59**, 1758 (1999).

[49] S. Grimme, Semiempirical GGA-type density functional constructed with a long-range dispersion correction, J. Comput. Chem. **27**, 1787 (2006).

[50] M. Leroux, I. Errea, M. Le Tacon, S.-M. Souliou, G. Garbarino, L. Cario, A. Bosak, F. Mauri, M. Calandra, and P. Rodiere, Strong anharmonicity induces quantum melting of charge density wave in 2*H*-$NbSe_2$ under pressure, Phys. Rev. B **92**, 140303(R) (2015).

[51] F. Giustino, M. L. Cohen, and S. G. Louie, Electron-phonon interaction using Wannier functions, Phys. Rev. B **76**, 165108 (2007).

[52] S. Poncé, E. R. Margine, C. Verdi, and F. Giustino, EPW: Electron–phonon coupling, transport and superconducting properties using maximally localized Wannier functions, Comput. Phys. Commun. **209**, 116 (2016).

[53] W. L. McMillan, Transition temperature of strong-coupled superconductors, Phys. Rev. **167**, 331 (1968).

[54] P. B. Allen and R. C. Dynes, Transition temperature of strong-coupled superconductors reanalyzed, Phys. Rev. B **12**, 905 (1975).

[55] P. B. Allen and B. Mitrović, Theory of superconducting T_c, Solid State Phys. **37**, 1 (1983).

[56] R. F. Frindt, Superconductivity in ultrathin $NbSe_2$ Layers, Phys. Rev. Lett. **28**, 299 (1972).

[57] H. Luo, J. Strychalska-Nowak, J. Li, J. Tao, T. Klimczuk, and R. J. Cava, S-shaped suppression of the superconducting transition temperature in Cu-intercalated $NbSe_2$, Chem. Mater. **29**, 3704 (2017).

[58] P. Baidya, V. Bagwe, P. Raychaudhuri, and A. Bid, Correlated carrier dynamics in a superconducting van der Waals heterostructure, Appl. Phys. Lett. **120**, 183101 (2022).

[59] E. Khestanova, J. Birkbeck, M. Zhu, Y. Cao, G. Yu, D. Ghazaryan, J. Yin, H. Berger, L. Forro, T. Taniguchi *et al.*, Unusual suppression of the superconducting energy gap and critical temperature in atomically thin $NbSe_2$, Nano Lett. **18**, 2623 (2018).

[60] C.-S. Lian, C. Heil, X. Liu, C. Si, F. Giustino, and W. Duan, Intrinsic and doping-enhanced superconductivity in monolayer 1*H*- TaS_2: Critical role of charge ordering and spin-orbit coupling, Phys. Rev. B **105**, L180505 (2022).

[61] S. Gołąb and B. Wiendlocha, Electron-phonon superconductivity in $CaBi_2$ and the role of spin-orbit interaction, Phys. Rev. B **99**, 104520 (2019).

[62] N. Troullier and J. L. Martins, Efficient pseudopotentials for plane-wave calculations, Phys. Rev. B **43**, 1993 (1991).

[63] K. Momma and F. Izumi, VESTA3 for three-dimensional visualization of crystal, volumetric and morphology data, J. Appl. Crystallogr. **44**, 1272 (2011).